Sub-nanometre pore adsorption of methane in kerogen

Sub-nanometre Pore Adsorption of Methane in Kerogen

Runxi Wang[a,b], Jun Li[c,], Livio Gibelli[a], Zhaoli Guo[b,], Matthew K. Borg[a,]

[a] *School of Engineering, Institute of Multiscale Thermofluids, The University of Edinburgh, Edinburgh EH9 3FB, UK*
[b] *State Key Laboratory of Coal Combustion, School of Energy and Power Engineering, Huazhong University of Science and Technology (HUST), Wuhan 430074, China*
[c] *Center for Integrative Petroleum Research, College of Petroleum Engineering and Geosciences, King Fahd University of Petroleum and Minerals, Dhahran 31261, Saudi Arabia*

Abstract

Developing unconventional shale gas resource has increased rapidly in recent years. However, while methane adsorbed inside organic kerogen matter is a source of shale production, it is still not a fully understood process. Here, we use molecular simulations to investigate methane adsorption in local micropores that are less than 1 nm inside realistic kerogen samples. We find an exponential scaling law for the local pore adsorption capacity and rationalise the pore density with the effective pore diameter, reservoir pressure, and sample porosity. This scaling law is determined from four kerogen samples at different porosities, each taken from a different shale reservoir, which have been experimentally validated in previous work. We find that pores closer to methane's diameter are responsible for ∼20% of the adsorption inside the sample and it is these small pores and lower pressures that dictate the largest adsorption capacity inside kerogen. Predictions of adsorption isotherms from properties of the kerogen structures are now possible using a proposed numerical percolation model by means of this scaling law. Adsorption predictions using our model show remarkably good agreement with molecular dynamics results in this work and isotherms in the

Email addresses: junli@kfupm.edu.sa (Jun Li), zlguo@hust.edu.cn (Zhaoli Guo), matthew.borg@ed.ac.uk (Matthew K. Borg)

literature, at a fraction of the computational cost. This work opens up a new route for determining adsorption isotherms of dense porous media from knowledge about their local pore structure, and can be scaled efficiently to support experimental campaigns, where molecular simulations would be intractable.

Keywords: shale, organic matter, adsorption isotherms, nanopores, molecular dynamics, percolation

---

1. Introduction

The shale gas revolution is transforming the world's energy landscape and increasing the shale gas exploration and production worldwide [1–3]. Due to the geological conditions of unconventional reservoirs and the complexity of adsorption and transport [4, 5], the production of shale gas is far from the forecast production [6, 7]. In unconventional reservoirs, the major storage of methane gas lies deep in the organic matter, known as kerogen, in an adsorbed state across various micropores (< 2 nm) and mesopores (< 50 nm) [8–11]. Mesopores have high pore volumes and can dominate the extraction process [12], however micropores have extremely high surface areas that leads to strong adsorption, albeit their accessible volume and contribution towards extraction are far from understood [13, 14].

There has been a recent drive to understand the relationship between methane adsorption and the kerogen's properties for better reservoir modelling and management. Gas adsorption isotherms of shale gas is the most common characterisation of a rock sample, usually measured by the manometric [15, 16], volumetric [17, 18] and gravimetric methods [19]. The Langmuir isotherm [20] is the most practical adsorption model used in the literature, which has also been shown to produce a good fit of the adsorption isotherms inside some, but not all, tight kerogen structures and pressures [21, 22]. Experiments or molecular simulations are normally used to determine the global response of adsorption in tight,

porous kerogen [21, 23, 23–27] under changes in reservoir conditions, most notably, pressure and temperature. There are also other influencing factors on adsorption, such as total organic carbon (TOC) content inside kerogen, which can lead to a stronger adsorption capacity of hydrocarbons [18], and kerogen maturity [28, 29], which can make the pores more tortuous, affecting porosity and connectivity of the pore network, and in turn the adsorption capacity of methane [30, 31]. Although we have a preliminary understanding of some of the influencing factors, we are still far from a) understanding the adsorption behaviour of methane in nanoscale pores of a complex kerogen structure and b) making reasonable predictions of adsorption in sub-core or core samples to match experiments.

Molecular dynamics (MD) simulation is a high fidelity tool that has been used successfully in the past to deeply explore the local adsorption behaviour that is normally difficult to capture in experiments. For example, using MD and the radial distribution function of methane near kerogen, it was found that methane molecules are more easily adsorbed near the sulfur and oxygen atoms of a kerogen sample [32, 33]. Furthermore, molecules prefer to be adsorbed on the hollow sites of the carbon ring of a hydrocarbon backbone [34]. In addition, characteristics of kerogen, such as surface roughness [35], pore size [36] and porosity [25] are known to play a role in adsorption. These studies have given us a qualitative understanding of the adsorption of methane at a microscopic level. Nevertheless, due to the complexity of the kerogen structure, in particular the vast heterogeneity, as well as the diversity of element types that exist, it is still currently challenging to quantitatively make reasonable predictions of the amount of shale gas adsorption in a complex kerogen structure that is embedded in a rock sample.

In this work, we use molecular dynamics to investigate methane adsorption

in micropores with sizes $D_{\text{pore}} \lesssim 10$ Å, which may be responsible for an important portion of adsorption in shale [13]. While grand canonical Monte Carlo (GCMC) simulations are common in the literature to measure the adsorption isotherms, here we opt for MD because gas adsorption is closer to the experiments [22], which requires excluding adsorption from the inaccessible pores [37]. Various techniques have been developed for building kerogen samples [38–40]. In our study, we use tight molecular kerogen structures from different geographic regions that have been experimentally calibrated in previous work [22], from which we measure the local densities in these pores ρ_{pore}. An exponential decay law is identified that describes how ρ_{pore} varies with D_{pore}, reservoir pressure P and sample porosity ϕ, with the latter playing a dominant role in the exponential decay. The exponential law can then be used to make efficient predictions of adsorption isotherms, for the first time, using percolation theory, provided the internal pore landscape is known.

2. Methodology

2.1. Molecular Dynamics (MD) simulations

Our MD simulations are run using the open-source molecular dynamics software LAMMPS [41]. Figure 1a shows a schematic of the MD set-up for methane adsorption measurements in kerogen. The set-up consists of a kerogen sample of cube dimensions $50 \times 50 \times 50$ Å^3 (initially empty) and placed in a semi-periodic system, with periodicity applied in the y and z directions. Reflective boundary conditions are applied in the x direction to avoid gas molecules from escaping the kerogen on the left edge of the simulation box, and we also verify that this modelling of the boundary does not produce any finite-size effects on the adsorption inside kerogen. A large reservoir of 2500 methane molecules is placed near one edge of the kerogen matrix (denoted as x^+ in Figure 1a), such that

filling occurs only from this edge. A piston is used to apply a pressure P on the reservoir of methane molecules. The piston is placed far from the kerogen entrance using a sufficiently large reservoir and only travels a short distance after adsorption. The reservoir dimensions can be calculated straightforwardly from the fixed number of molecules in the reservoir and the target pressure/density; for example, the reservoir length at 50 MPa is 135 Å.

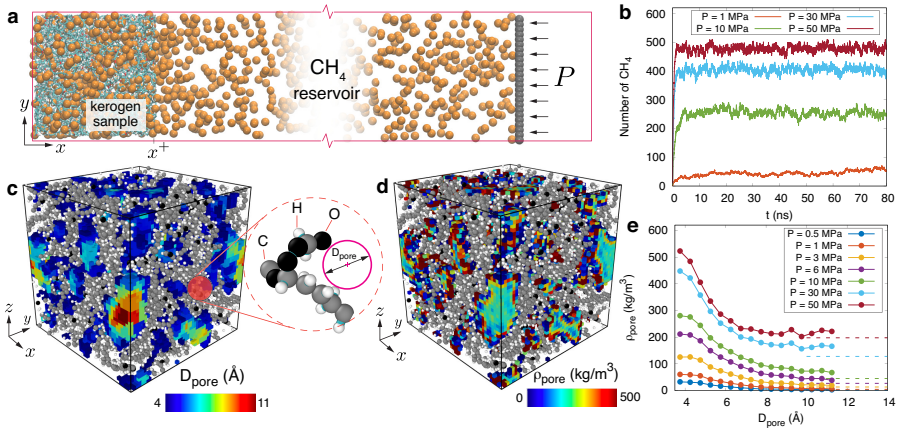

Figure 1: a) MD simulation set-up for CH_4 adsorption under constant pressure P. Color code: methane (orange), carbon (cyan), oxygen (red), hydrogen (white), piston (gray). b) Time evolution of the number of methane molecules adsorbed inside the EFK 0.8 g/cm^3 kerogen for selected pressures. c) Pore sizes of EFK 0.8 g/cm^3 kerogen; small pores (< 3 Å) are omitted from the calculation. The Voronoi grid is used here first to measure D_{pore} and is mapped to a Cartesian grid for visualisation (see SI for details). d) Methane density measurements in the EFK 0.8 g/cm^3 kerogen at 50 MPa on a Cartesian grid. e) Distribution of local pore density with pore size under different pressures. The horizontal dashed lines are the bulk reservoir densities ρ_{bulk} at the respective pressure.

In this work, eight different kerogen samples are used, which were obtained

from Bousige et al. [22]. These molecular structures were built by combining hybrid reverse Monte Carlo and MD simulations [42] to be consistent with the experimental data, such as in matching the C–C pair distribution functions, pore size distribution and elastic properties. These samples have two different densities (0.8 g/cm^3 and 1.0 g/cm^3) and come from four different regions, including the Middle East kerogen (MEK), Eagle Ford field kerogen (EFK), the Marcellus field kerogen (MarK), and a kerogen-like shungite from Russia (PY02), with their maturity increasing in the order listed. These lower density kerogen samples are selected to improve the sampling statistics of local pore adsorption measurements because of their larger pore networks and connectivity, as they contain a larger range of pore sizes as well as more adsorbed molecules. These chosen samples also span porosities between $\phi = 30\%$ – 55%, noting that it is unrealistic to have internal connections when the porosity is lower than 23% [21]. Therefore, our analysis in this work is expected to be valid for low porous surfaces, with $\phi > 23\%$. The eight kerogen samples are listed in Table 1, including their elemental composition and porosity. All other details regarding the experimental calibration, characterisation and validation of these samples can be found in the work of Bousige et al. [22], such as Table SI1 in that paper.

The intermolecular force fields and MD integration conditions in this work are similar as those considered in References [21, 22, 25]. The equations of motion of all molecules, except the kerogen atoms, which are modelled as rigid, are numerically integrated using the velocity Verlet algorithm with a time-step of 2 fs, a neighbour list cut-off radius of $r_{\text{cut}} = 20$ Å and using the Lennard Jones (LJ) potential between different species of atoms:

$$U_{\text{LJ}} = 4\epsilon_{\alpha\beta}\left[\left(\frac{\sigma_{\alpha\beta}}{r_{\alpha\beta}}\right)^{12} - \left(\frac{\sigma_{\alpha\beta}}{r_{\alpha\beta}}\right)^{6}\right], \tag{1}$$

where $\sigma_{\alpha\beta}$ and $\epsilon_{\alpha\beta}$ are the length and energy characteristics of the potential

Density	Type	C	H	O	ϕ
0.8 g/cm^3	EFK	3849	4246	298	45%
	MEK	3995	4889	300	42%
	MarK	3883	1442	328	50%
	PY02	4911	422	41	56%
1.0 g/cm^3	EFK	4890	5395	411	35%
	MEK	5019	6064	388	31%
	MarK	5160	2026	507	41%
	PY02	6134	514	44	46%

Table 1: Elemental composition and number of constituent atoms inside each kerogen sample considered in this work [22] and porosity ϕ measurements obtained from Ref. [21].

between two species (α, β), and $r_{\alpha\beta}$ is the distance between two atoms. For methane, we use a coarse-grained, single-site model [43] that interacts with all atoms in the system with LJ parameters given in Table 2. This methane model has been validated and calibrated in previous work to describe the properties of methane as well as its adsorption in kerogen as shown by experiments [21, 22, 25].

The piston is modelled as a single degrees of freedom body that moves only in the x direction. Each atom on the piston is acted upon by a constant force pointing in the negative x direction, given by $F = PA/N$, where A is the area of the piston and $N = 625$ is the number of piston wall atoms. The atoms on the piston are uniformly distributed and their spacing (2 Å) is small enough to prevent gas molecules from permeating through at large pressures. The mass of the piston is kept low, by having a one-atom-thick sheet with each atom having the same mass as carbon, in order to prevent the pressure overshooting inside the reservoir during the adsorption process. The interaction between the piston molecules and methane is artificially made weak to prevent methane molecules from adsorbing on the piston surface. As the piston never comes within interaction range of the kerogen, the LJ parameters between piston and kerogen are also artificial.

Molecule pairs	$\epsilon_{\alpha\beta}$ (kcal/mol)	$\sigma_{\alpha\beta}$ (Å)
CH_4-CH_4	0.2941	3.730
CH_4-C	0.1279	3.545
CH_4-O	0.2135	3.450
CH_4-H	0.0936	3.075
CH_4-P	0.0050	2.500
C-C	0.0556	3.360
O-O	0.1550	3.170
H-H	0.0298	2.420

Table 2: Lennard Jones parameters for the kerogen atoms (C, H, O), methane (CH_4) and piston (P). Lorentz-Berthelot rules were used to calculate the interactions between different elements, while the interaction potential parameters between methane and the piston are artificial. We include the C-C, O-O, and H-H potential parameters for completeness, but these atoms are kept rigid during the simulation.

In the adsorption simulations, the reservoir pressures and temperature were set to those expected in shale. Pressure was varied between $P = 1$–50 MPa using the piston, while temperature was kept constant at 423 K in an NVT ensemble using the Nosé-Hoover thermostat with a relaxation time of 0.1 ps [44]. Our simulation procedure involved a number of steps. With the kerogen remaining empty, the gas in the reservoir was equilibrated to the target pressure for around 3 ns using the piston. This allows any minor oscillations in the motion of the piston to settle down. The initial density state of methane inside the reservoir is also set equal to the target pressure, which means the piston is already in the right position to begin with and its motion during this equilibration stage is small. Furthermore, as mentioned above, the inertia of the piston is low, which avoids any large overshoots during its motion [45]. Measurements for pressure and density in the bulk of the reservoir after equilibration agree with the bulk properties of methane obtained from the National Institute of Standards and Technology (NIST) database [46], confirming the correct implementation of the

piston method.

The kerogen side connected to the reservoir is then opened and methane molecules are allowed to adsorb inside the kerogen sample under constant pressure for a duration of approximately 60 ns. Figure 1b shows an example of the time evolution of methane molecules recorded inside the kerogen, for a few selected pressures. While the adsorption process is dynamic, the pressure in the reservoir remains constant, and the piston rapidly reaches its new position to account for the loss in mass. The distance the piston travels is minimised by setting the reservoir to contain more than 5 times the mass of what is lost to the kerogen during adsorption. Measurements for adsorption, as detailed in the next sections, are all initiated after all transients die out and steady-state is reached.

2.2. Pore adsorption measurements

Confinement in simple slits [12, 47] or cylindrical tubes [48–50] has a major effect on adsorption, with pore density increasing with decreasing pore size. However, the tortuous micropores inside kerogen makes the analysis and prediction of local adsorption much more challenging. In particular, the form of this pore-density/pore-size relationship is expected to decay differently due to a number of factors, such as in differences of ordering and packing of gas inside slits or cylindrical tube geometries, with surfaces which are often modelled using pristine structures, and the potential energy field experienced by molecules inside a porous kerogen matrix being hard to replicate in these simplified test cases.

In this work, the pore landscape is resolved by a three-dimensional Voronoi grid [51] applied to the empty space between kerogen atoms, where a single pore is a sphere centred at a Voronoi grid node in the interstices of the kerogen atoms (see inset in Figure 1c). Each Voronoi sphere has a diameter D_{pore},

which does not overlap with any kerogen atoms, and is defined as the distance between the closest kerogen atoms and the centre of the Voronoi sphere, but subtracting the methane-kerogen van der Waals diameter $\sigma_{\mathrm{CH_4-x}}$ ($\mathrm{x} = \mathrm{C}, \mathrm{H}, \mathrm{O}$). Pore adsorption is measured by the occupancy of molecules inside these pores throughout the duration of the MD simulation. We found that the amount of adsorption inside flexible and rigid kerogen models is very similar. However, the choice of using a rigid kerogen has the advantage that the grids we use for measuring local pore adsorption (which are computationally expensive to build) are defined and built once. If a flexible kerogen model was adopted, these will need to be built at each MD timestep. More details on calculating the pores from the Voronoi grid and the measurement of local pore adsorption density are given in the Supplementary Information (SI).

3. Results and discussion

3.1. Sub-nanometre pore adsorption capacity

Figure 1c shows an example of the pore sizes D_{pore} obtained from the Voronoi grid, projected on a Cartesian grid for the EFK 0.8 g/cm^3 kerogen sample, while Figure 1d shows the corresponding measurement of pore densities ρ_{pore} from the MD simulation using the Cartesian grid. Although statistical noise is evident in the MD measurements of density, methane adsorption can be seen to be lower in larger pores, and higher in smaller ones, if the two figures are compared qualitatively. This result is consistent with previous studies on slit nanopores and carbon nanotubes [47, 48, 52, 53], which, while not being similar to the porous kerogen structures considered here, also reflects the stronger adsorption of gas molecules by smaller pores.

After obtaining D_{pore} and ρ_{pore} in the 3D samples, we analysed further the adsorption of methane in each of the pores by averaging the density for all

similar sized pores; these results are shown in Figure 1e. This figure shows that methane adsorption in kerogen gradually decreases with increasing pore size, and approaches the bulk reservoir density for larger pore sizes. Under higher reservoir pressures, the amount of adsorption also increases inside the pores, as expected by the Langmuir isotherm.

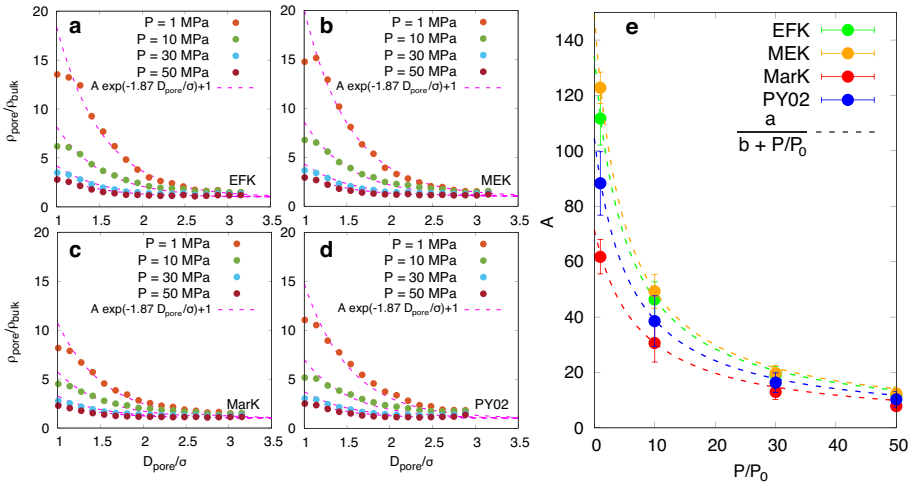

Figure 2: Normalized adsorption density with bulk density ($\rho_{\text{pore}}/\rho_{\text{bulk}}$) as a function of D_{pore}/σ, where $\sigma = \sigma_{\text{CH}_4}$, under different pressures P for the following 0.8 g/cm^3 kerogen samples: a) EFK, b) MEK, c) MarK, d) PY02. The dashed line is the exponential decay curve from Eq. (2) fitted for parameter A. e) A as a function of normalized pressure for the four samples. The dashed lines in e) are fitted using Eq. (3).

In order to rationalise a relationship between the local density and pore size for all kerogen samples, the density distribution in Figure 1e is normalized with the bulk reservoir density ρ_{bulk}. Figure 2 shows the normalized pore density distributions of EFK (Fig. 2a), MEK (Fig. 2b), MarK (Fig. 2c) PY02 (Fig. 2d) for the kerogen sample at 0.8 g/cm^3, while the equivalent profiles for all 1.0 g/cm^3 samples are given in the SI. The normalised pore densities of the four

different samples show three key observations: (1) the local pore densities follow a similar behaviour in which they are exponentially decreasing with pore size and approach $\rho_{\text{pore}}/\rho_{\text{bulk}} = 1$ at large pore sizes; (2) the exponential flattens out at the highest pressure, which indicates the adsorption inside most pores are closer to the density of bulk fluid; and (3) in contrast to the result before normalization, the normalized adsorption under low pressure is highest, which clearly indicates that sub-nanometre pores in kerogen have a relatively stronger adsorption capacity of methane at low reservoir pressures. This occurs because the rate of increase in adsorption density inside the pores, which is dominated by the kerogen's force field, does not match the rate of density increases in the reservoir, which is dominated by the fluid thermodynamics. The attractive part of the force field is what initially drives adsorption in the low pressure limit. However, the repulsive part determines whether methane molecules are adsorbed closer to the internal surface or percolate throughout the connected pore space of the sample through the tight throat sections that exist, which is gradually overcome at higher pressures.

3.2. Pore-adsorption scaling law

In this work, we propose the following exponential function to describe the normalized pore density for all the kerogen samples:

$$\frac{\rho_{\text{pore}}}{\rho_{\text{bulk}}} = A \exp\left(\frac{-1.87\ D_{\text{pore}}}{\sigma_{\text{CH}_4}}\right) + 1, \tag{2}$$

where A is the degree of methane adsorption in pores under an applied pressure, and is dependent on the kerogen properties, $\sigma_{\text{CH}_4} = 3.73$ Å is the van der Waals diameter of methane, and the constant 1.87 is a fitted term averaged across all simulations and then fixed when fitting for A. Figures 2a-d show that the expression in Eq. (2) can fit the four different kerogen types very well under

different pressures. The densities in the smallest pores were found to deviate slightly from the fitted curve at low pressures, which occur because their pore sizes are close to, or smaller than, the limit of adsorption, i.e. $\sim \sigma_{CH_4}$. We find that these small pores ($D_{\text{pore}} < 4$Å) can store ∼20% of the molecular adsorption in the sample, and a ∼5% error in the final adsorption capacity evaluation is expected as a result of these observed deviations. Despite changes in kerogen type, maturity and porosity in the samples considered in this work, the degree of adsorption A behaves very similarly with pressure in Figure 2e, which follows the functional form:

$$A = \frac{a}{b + P/P_0}, \tag{3}$$

where a and b do not change with pressure P (defined here in MPa), and P_0 is a reference pressure taken here as the lowest considered pressure (1 MPa). In recent work [21], the diffusion of methane inside kerogen was found to depend on porosity and a number of other physicochemical properties, such as kerogen-methane friction coefficient, packing efficiency and cavity overlap coefficient, which all in turn depend on porosity. Here, we similarly find that porosity also plays a key role on adsorption. Figures 3a,b show the relationship between the porosity of different types of kerogen and the parameters a and b. Parameter a is proportional to A, representing the degree of adsorption of methane, and therefore strongly related to porosity, as shown in Figure 3a. This is confirmed in Figure 4, where we find the lower porosity samples (1.0 g/cm^3) have a higher probability of smaller pores and stronger attractive energies than the equivalent pores of the higher porous samples. In contrast, the variation of parameter b has little effect on A and therefore the adsorption capacity. It can be considered as a constant, or slowly increasing with porosity, as we consider here.

The strength of adsorption may also be affected by the composition of chemical elements that make up the kerogen. For example, the pyrobitumen PY02

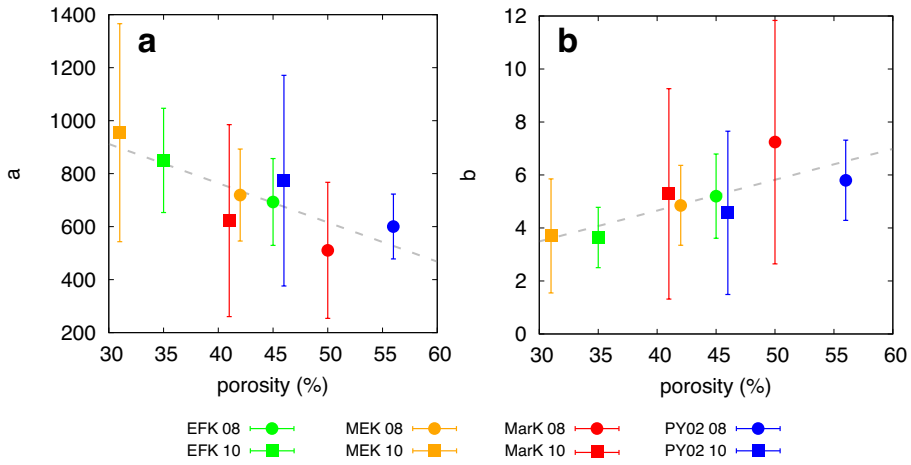

Figure 3: a) Adsorption parameter a from Eq. (3) as a function of porosity ($a = -14.8\ \phi + 1356$). b) Adsorption parameter b from Eq. (3) as a function of porosity ($b = 0.1164\ \phi$); note that the critical porosity is $\phi_c \approx 23\%$, below which no connectivity exists inside the kerogen to drive adsorption internally [21]. The colors in the figures represent different types of kerogen (green = EFK; orange = MEK; red = MarK; blue = PY02), the circle symbol represents the kerogen with a density of 0.8 g/cm^3, and the square symbol represents the kerogen with a density of 1.0 g/cm^3.

sample with the largest porosity ($\phi = 56\%$) has a very low hydrogen-carbon ratio (<1%) because of its high maturity. In comparison with the MarK kerogen, the porosity is similar ($\phi = 50\%$) but the hydrogen-carbon ratio is larger (8.4%). Since the carbon atoms have a stronger adsorption for methane than the hydrogen atoms, the adsorption capacity of PY02 is stronger than the MarK kerogen, indicating A will be larger (see Figure 2e). Pore potential energy measurements (see method in SI) in Figure 4 also show that the adsorption capacity of PY02 is stronger than MarK for the same pore size.

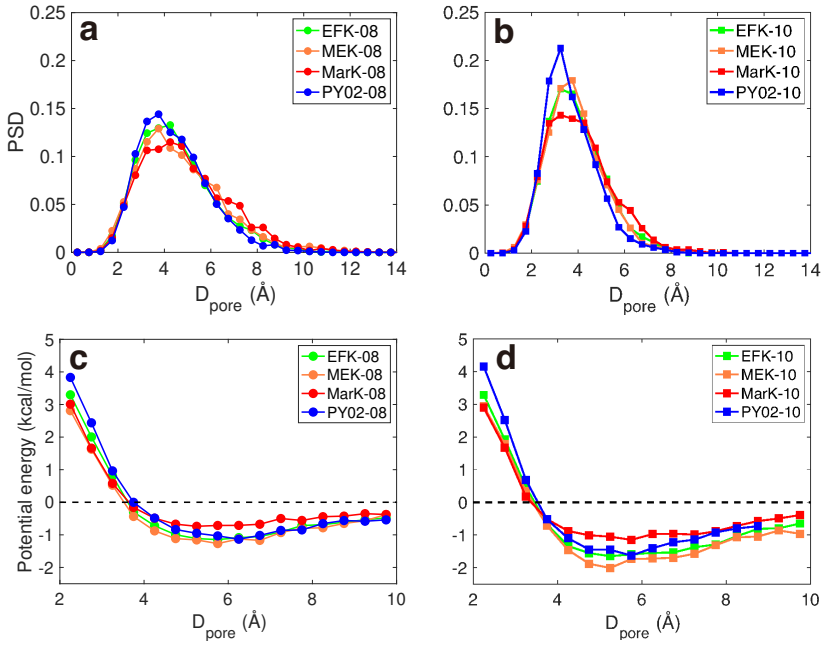

Figure 4: Pore size distribution (PSD) for the kerogen samples considered in this work with densities: (a) 0.8 g/cm^3 and (b) 1.0 g/cm^3. Pore potential energy of methane in kerogen as a function of pore size D_{pore} for densities: (c) 0.8 g/cm^3 and (d) 1.0 g/cm^3.

3.3. Percolation model for adsorption

Despite molecular dynamics being the benchmark solver for modelling adsorption/desorption processes in kerogen, here we propose using percolation theory [54] to make efficient predictions of adsorption using the empirical law given by Eqs. (2) and (3). Our percolation model (PM), summarised in the flow diagram in Figure 5, requires a pore structure of a 3D sample, and uses a Cartesian grid with pore diameters projected from the Voronoi grid (see Figure 1c). Gas can percolate either from one side, as the MD simulations carried out in this work, or from any number of the six available sides of the cubic sample.

Two input parameters are required to run the percolation simulation: (i) the minimum pore size for percolation $D_{\min}$, which is a fixed input value to the model, and (ii) the adsorption capacity in Eq. (2), with fitting equations for $a = -14.8\ \phi + 1356$ and $b = 0.1164\ \phi$ (where porosity $\phi > 23\%$ for percolation [21]), and $\rho_{\text{bulk}}(P)$ taken from the NIST database [46].

The PM simulation proceeds as follows, with an example shown in Figures 5a-c. The sides to percolate are initially chosen on the sample. To match the MD simulations conducted in this work, we pick only the x^+ side for adsorption, although we also carry out percolation simulations for all six sides below to match adsorption isotherms obtained from literature simulations. The PM algorithm attempts gas filling through the first layer of Cartesian cells on that boundary (see Figure 5a). If a cell's pore size is greater than $D_{\min}$, then that cell gets filled with its associated pore density ρ_{pore} from Eq. (2).

For each percolated cell, all neighbouring cells are attempted to be filled in an iterative manner, with the algorithm keeping track of which cells have already been tested purely for computational efficiency. Once no more neighbour cells are available to percolate at a particular iteration step, the percolation simulation finishes (see Figure 5c). The total sample adsorption, which can

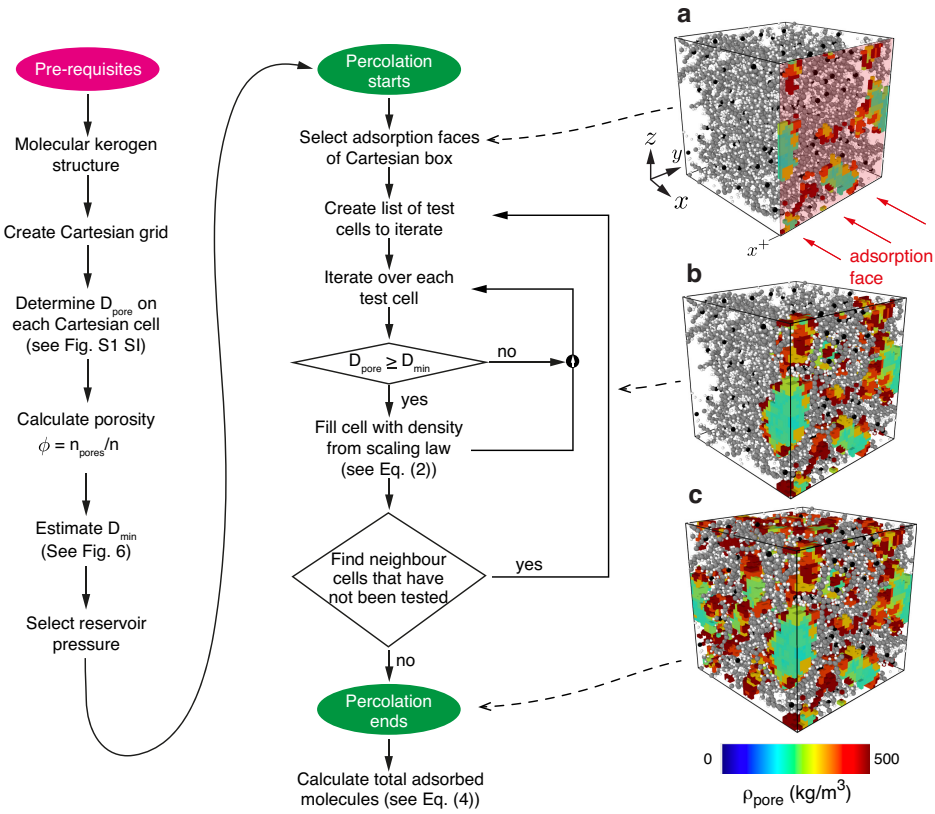

Figure 5: Flow chart summarising the proposed percolation model. Note, porosity is calculated as the ratio of free accessible volume to the total volume, which can be obtained from the cartesians cells in Fig. 1c, with n_{pores} being all the coloured cells ($D_{\text{pore}} > \sigma_{\text{CH}_4}$) and n is the total number of cartesian cells. Figures a-c correspond to different iterations of the PM adsorption simulation for a case corresponding to EFK 0.8 g/cm^3 kerogen at pressure $P = 50$ MPa. Specifically, iteration a) 1, b) 10, and c) 70. The adsorption face is indicated at x^+, and cells are coloured by pore density.

be dictated in terms of number of methane molecules, can be calculated by summing the local methane adsorption for all filled cells as follows:

$$N_{\mathrm{CH_4}}(P) = \sum_{i=1}^{n} \rho_i V_i, \tag{4}$$

where ρ_i, V_i is the density and volume of an arbitrary Cartesian cell and n is the total number of cells adsorbed by methane.

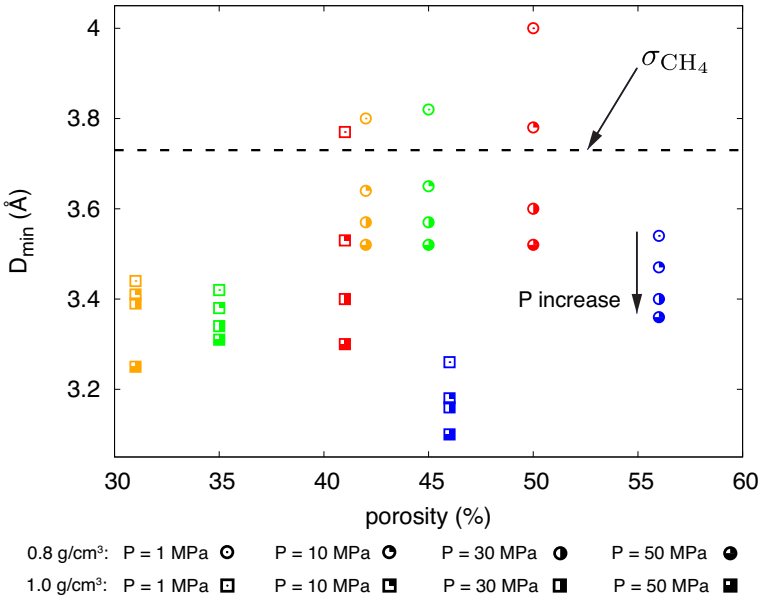

Figure 6: The smallest pore diameter that a methane molecule can pass through the interstitial kerogen matrix (defined as D_{min}) as a function of porosity. The diameter of methane ($\sigma_{\mathrm{CH_4}}$) is indicated by the horizontal dashed line and the blue arrow indicates the direction of increase in reservoir pressure (1, 10, 30, 50 MPa). The colors in the figure represent different types of kerogen (green = EFK; orange = MEK; red = MarK; blue = PY02), the circle symbols represent the kerogen with a density of 0.8 g/cm^3, and the square symbols represent the kerogen with a density of 1.0 g/cm^3.

In order to run the PM simulations, we require defining the minimum pore diameter $D_{\min}$ that allows percolation of methane through the 3D pores. Estimates of $D_{\min}$ are calibrated from the MD simulations, and are shown in Figure 6 (see SI for method and data). As expected, we find that the value of $D_{\min}$ is approximately the diameter of methane ($\sigma_{CH_4} = 3.73$ Å), but depends on pressure, kerogen element composition and tight confinement. This occurs because methane molecules at higher pressure have more probability to overcome the energy barrier through the throat-like connections in the pore network, and as seen in Figure 4, pore potential energies are slightly dependent on kerogen density and chemical composition. Except for the highest maturity pyrobitumen PY02 sample, the minimum percolation lengthscale of the other three kerogen samples are close to each other. As mentioned earlier, the kerogen-like shungite in the PY02 sample contains less hydrogen atoms, and the atoms on the surface of the throat are mostly carbon instead of hydrogen, thereby increasing the energy barrier for percolation and lowering $D_{\min}$. Confinement also seems to play a small role, with the 0.8 g/cm^3 (high porosity) samples having a seemingly larger $D_{\min} \sim 3.5$ Å than the 1.0 g/cm^3 samples, which is $D_{\min} \sim 3.3$ Å. This reflects the previous observation that lower porosity samples have higher local adsorption strength, and therefore allow percolation through smaller pore sizes.

Figures 7a–d show the comparison between the adsorption isotherms of the eight kerogen samples predicted by the PM simulations, which we find are in good agreement with our MD results and also follow Langmuir's law. There are also large computational savings when running the PM simulations. Compared with the MD simulation, which requires one day (on 24 CPU cores) to obtain a single data point on the adsorption isotherm plot of 5–10 data points, the percolation simulation takes about 20 minutes (on one CPU core) to predict a complete adsorption isotherm curve, with the major cost arising from generating

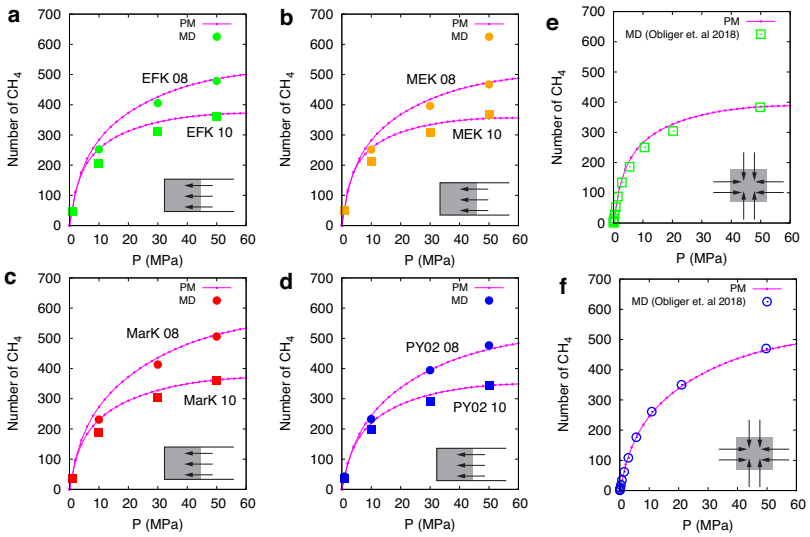

Figure 7: Adsorption simulations between PM and MD results for kerogen samples: a) EFK (green), b) MEK (orange), c) MarK (red), d) PY02 (blue). Circle and square symbols are the molecular dynamics results for kerogen densities of 0.8 g/cm^3 and 1.0 g/cm^3, respectively, while the purple lines are the corresponding predictions from our percolation model. $D_{\min} = 3.5$ Å for kerogen with 0.8 g/cm^3 and the $D_{\min} = 3.3$ Å for kerogen with 1.0 g/cm^3, while PY02 samples use 3.4 Å and 3.1 Å, respectively. Comparisons in e) and f) are for EFK-10 and the PY02-08 MD adsorption results taken from Ref. [21] (empty symbols). In Figures a–d the kerogen structures are filled from the positive x side, while Figures e,f are filled from all six sides, as indicated by the inset.

the internal pore grids from the kerogen matrix.

To further validate our method, we obtained adsorption MD data points from Obliger et al. [21] for two kerogen samples. These MD simulations were allowed to adsorb from all six sides of the kerogen box, making adsorption different to our results due to the connectivity inside the samples. The predicted results from our percolation model agreed well with their MD results, as shown in Figures 7e,f. This shows that the exponential adsorption law has promise to be universal, at least for the samples and data that were available to us, while the percolation method shows similar promise to make reasonable estimates of adsorption isotherms of new or large kerogen samples that are not affordable to simulate using MD.

4. Conclusions

We have investigated the adsorption of methane in sub-nanometre pores of organic kerogen. We found a universal relationship that rationalises pore density with pore size, pressure and porosity. Small pores at low reservoir pressures were found to have the strongest adsorption capacity, with adsorption capacity found to decrease exponentially with increasing pore size, and scales linearly with porosity and the inverse of pressure. A percolation model is presented, which is 3–4 orders of magnitude less computationally demanding than traditional molecular dynamics simulations, and is scalable to model larger samples in experiments, where heterogeneity exists. Besides the universal law for pore density developed in this work, the PM requires input of atomic positions of the kerogen structure, and an estimate of the minimum percolation pore diameter $D_{\min}$ to make predictions of adsorption isotherms. We found that $D_{\min}$ is not a fixed value and has no apparent scaling law, although we do observe that it varies with porosity and pressure and does not change more than approximately ± 0.5

Å from the size of the molecular diameter. Furthermore, since $D_{\min}$ is calculated on the diameter of methane, it is not expected to be effected by other chemical elements, such as sulfur or nitrogen, which are also sometimes found in kerogen.

This work provides a new route for determining adsorption isotherms of dense porous media from knowledge about their local pore structure, and can be scaled efficiently to support experimental campaigns, where molecular simulations would be intractable. The relationships obtained in this work relate the porosity of a kerogen sample to its adsorption, which means these simplified laws could also be used to support future transport models, where adsorption determines hydrocarbon diffusivity in kerogen [21]. Additional studies can be carried out to identify laws that relate swelling in the kerogen structure to pressure. These laws could then be used as input to refine the adsorption isotherms in the percolation simulation method for high pressures. Beyond shale gas, this work can be extended to other research areas involving adsorption in nanoporous media, such as in electrochemical adsorption and energy storage, which may require investigation of how Coulombic charges between electrodes and electrolyte fluids impact the scaling law for adsorption on porosity we found here.

Acknowledgements

This work was financial supported by King Fahd University of Petroleum and Minerals (KFUPM), Saudi Arabia. All MD simulations were run on ARCHER, the UK's national supercomputing service. MKB and LG thank support from the Engineering and Physical Sciences Research Council (EP/N016602/1 and EP/R007438/1). ZG and RW thank support from the National Science Foundation of China (51836003). RW also thanks support from Sichuan Science and Technology Program (No. 2019YFG0457). The authors would like to thank Colin Bousige (and co workers) for providing us the kerogen structures used in

this work.

Supporting Information

Other supporting methods and results are available at *(DOI to be added here at proofs stage that links to the Supplementary Information document).*

References

[1] R. A. Kerr, Natural gas from shale bursts onto the scene, Science 328 (5986) (2010) 1624–1626.

[2] D. M. Kargbo, R. G. Wilhelm, D. J. Campbell, Natural gas plays in the marcellus shale: Challenges and potential opportunities, Environmental Science and Technology 44 (15) (2010) 5679–5684.

[3] C. McGlade, J. Speirs, S. Sorrell, Unconventional gas - A review of regional and global resource estimates, Energy 55 (2013) 571–584.

[4] Z. Li, J. Yao, J. Kou, Mixture composition effect on hydrocarbon–water transport in shale organic nanochannels, The Journal of Physical Chemistry Letters 10 (15) (2019) 4291–4296.

[5] A. Phan, A. Striolo, Evidence of facilitated transport in crowded nanopores, The Journal of Physical Chemistry Letters 11 (5) (2020) 1814–1821.

[6] J. D. Hughes, A reality check on the shale revolution, Nature 494 (7437) (2013) 307–308.

[7] L. Cueto-Felgueroso, R. Juanes, Forecasting long-term gas production from shale, Proceedings of the National Academy of Sciences of the United States of America 110 (49) (2013) 19660–19661.

[8] Y. Yang, J. Liu, J. Yao, J. Kou, Z. Li, T. Wu, K. Zhang, L. Zhang, H. Sun, Adsorption behaviors of shale oil in kerogen slit by molecular simulation, Chemical Engineering Journal 387 (2020) 124054.

[9] Z. Sun, X. Li, W. Liu, T. Zhang, M. He, H. Nasrabadi, Molecular dynamics of methane flow behavior through realistic organic nanopores under geologic shale condition: Pore size and kerogen types, Chemical Engineering Journal 398 (2020) 124341.

[10] M. Vandenbroucke, C. Largeau, Kerogen origin, evolution and structure, Organic Geochemistry 38 (5) (2007) 719–833.

[11] Y. Ju, J. He, E. Chang, L. Zheng, Quantification of ch4 adsorption capacity in kerogen-rich reservoir shales: An experimental investigation and molecular dynamic simulation, Energy 170 (2019) 411–422.

[12] F. Guo, S. Wang, Q. Feng, X. Yao, Q. Xue, X. Li, Adsorption and absorption of supercritical methane within shale kerogen slit, Journal of Molecular Liquids 320 (2020) 114364.

[13] M. Mastalerz, A. Schimmelmann, A. Drobniak, Y. Chen, Porosity of devonian and mississippian new albany shale across a maturation gradient: Insights from organic petrology, gas adsorption, and mercury intrusion, AAPG Bulletin 97 (10) (2013) 1621–1643.

[14] H. Tian, L. Pan, X. Xiao, R. W. Wilkins, Z. Meng, B. Huang, A preliminary study on the pore characterization of lower silurian black shales in the chuandong thrust fold belt, southwestern china using low pressure n2 adsorption and fe-sem methods, Marine and Petroleum Geology 48 (2013) 8–19.

[15] P. Weniger, W. Kalkreuth, A. Busch, B. M. Krooss, High-pressure methane

and carbon dioxide sorption on coal and shale samples from the Paraná Basin, Brazil, International Journal of Coal Geology 84 (3-4) (2010) 190–205.

[16] T. F. Rexer, M. J. Benham, A. C. Aplin, K. M. Thomas, Methane adsorption on shale under simulated geological temperature and pressure conditions, Energy and Fuels 27 (6) (2013) 3099–3109.

[17] W. Yu, K. Sepehrnoori, T. W. Patzek, Modeling gas adsorption in marcellus shale with langmuir and bet isotherms, SPE Journal 21 (2) (2016) 589–600.

[18] T. Zhang, G. S. Ellis, S. C. Ruppel, K. Milliken, R. Yang, Effect of organic-matter type and thermal maturity on methane adsorption in shale-gas systems, Organic Geochemistry 47 (2012) 120–131.

[19] S. Zhou, H. Xue, Y. Ning, W. Guo, Q. Zhang, Experimental study of supercritical methane adsorption in Longmaxi shale: Insights into the density of adsorbed methane, Fuel 211 (2018) 140–148.

[20] I. Langmuir, The adsorption of gases on plane surfaces of glass, mica and platinum, Journal of the American Chemical Society 40 (9) (1918) 1361–1403.

[21] A. Obliger, F. J. Ulm, R. Pellenq, Impact of Nanoporosity on Hydrocarbon Transport in Shales' Organic Matter, Nano Letters 18 (2) (2018) 832–837.

[22] C. Bousige, C. M. Ghimbeu, C. Vix-Guterl, A. E. Pomerantz, A. Suleimenova, G. Vaughan, G. Garbarino, M. Feygenson, C. Wildgruber, F. J. Ulm, R. J. Pellenq, B. Coasne, Realistic molecular model of kerogen's nanostructure, Nature Materials 15 (5) (2016) 576–582.

[23] L. Chen, L. Zuo, Z. Jiang, S. Jiang, K. Liu, J. Tan, L. Zhang, Mechanisms of shale gas adsorption: Evidence from thermodynamics and kinetics study

of methane adsorption on shale, Chemical Engineering Journal 361 (2019) 559–570.

[24] K. Falk, B. Coasne, R. Pellenq, F. J. Ulm, L. Bocquet, Subcontinuum mass transport of condensed hydrocarbons in nanoporous media, Nature Communications 6 (2015) 1–7.

[25] A. Obliger, R. Pellenq, F. J. Ulm, B. Coasne, Free Volume Theory of Hydrocarbon Mixture Transport in Nanoporous Materials, Journal of Physical Chemistry Letters 7 (19) (2016) 3712–3717.

[26] J. Zou, R. Rezaee, K. Liu, Effect of temperature on methane adsorption in shale gas reservoirs, Energy & Fuels 31 (11) (2017) 12081–12092.

[27] K. Lin, X. Huang, Y.-P. Zhao, Combining image recognition and simulation to reproduce the adsorption/desorption behaviors of shale gas, Energy & Fuels 34 (1) (2020) 258–269.

[28] H. Sui, F. Zhang, Z. Wang, D. Wang, Y. Wang, Effect of kerogen maturity, water content for carbon dioxide, methane, and their mixture adsorption and diffusion in kerogen: A computational investigation, Langmuir 36 (33) (2020) 9756–9769.

[29] T. Zhao, X. Li, H. Zhao, M. Li, Molecular simulation of adsorption and thermodynamic properties on type II kerogen: Influence of maturity and moisture content, Fuel 190 (2017) 198–207.

[30] J. Berthonneau, A. Obliger, P.-L. Valdenaire, O. Grauby, D. Ferry, D. Chaudanson, P. Levitz, J. J. Kim, F.-J. Ulm, R. J.-M. Pellenq, Mesoscale structure, mechanics, and transport properties of source rocks' organic pore networks, Proceedings of the National Academy of Sciences 115 (49) (2018) 12365–12370.

[31] V. Agrawal, S. Sharma, Are we modeling the properties of unconventional shales correctly?, Fuel 267 (2020) 117316.

[32] H. Sui, J. Yao, Effect of surface chemistry for CH4/CO2 adsorption in kerogen: A molecular simulation study, Journal of Natural Gas Science and Engineering 31 (2016) 738–746.

[33] L. Huang, Z. Ning, Q. Wang, W. Zhang, Z. Cheng, X. Wu, H. Qin, Effect of organic type and moisture on CO2/CH4 competitive adsorption in kerogen with implications for CO2 sequestration and enhanced CH4 recovery, Applied Energy 210 (2018) 28–43.

[34] H. Sun, H. Zhao, N. Qi, Y. Li, Molecular Insights into the Enhanced Shale Gas Recovery by Carbon Dioxide in Kerogen Slit Nanopores, Journal of Physical Chemistry C 121 (18) (2017) 10233–10241.

[35] T. Wu, A. Firoozabadi, Fracture Toughness and Surface Energy Density of Kerogen by Molecular Dynamics Simulations in Tensile Failure, The Journal of Physical Chemistry C 124 (29) (2020) 15895–15901.

[36] G. Chen, S. Lu, K. Liu, Q. Xue, C. Xu, S. Tian, J. Li, Y. Zhang, M. Tong, X. Pang, B. Ni, S. Lu, Q. Qi, Investigation of pore size effects on adsorption behavior of shale gas, Marine and Petroleum Geology 109 (2019) 1–8.

[37] L. Michalec, M. Lísal, Molecular simulation of shale gas adsorption onto overmature type II model kerogen with control microporosity, Molecular Physics 115 (9-12) (2017) 1086–1103.

[38] B. Zhou, R. Xu, P. Jiang, Novel molecular simulation process design of adsorption in realistic shale kerogen spherical pores, Fuel 180 (2016) 718–726.

[39] Z. Sun, X. Li, W. Liu, T. Zhang, M. He, H. Nasrabadi, Molecular dynamics of methane flow behavior through realistic organic nanopores under geologic shale condition: Pore size and kerogen types, Chemical Engineering Journal 398 (2020) 124341.

[40] S. Wang, X. Yao, Q. Feng, F. Javadpour, Y. Yang, Q. Xue, X. Li, Molecular insights into carbon dioxide enhanced multi-component shale gas recovery and its sequestration in realistic kerogen, Chemical Engineering Journal 425 (2021) 130292.

[41] S. Plimpton, Fast parallel algorithms for short-range molecular dynamics, Journal of Computational Physics 117 (1) (1995) 1–19.

[42] C. Bousige, A. Boţan, F.-J. Ulm, R. J.-M. Pellenq, B. Coasne, Optimized molecular reconstruction procedure combining hybrid reverse monte carlo and molecular dynamics, The Journal of Chemical Physics 142 (11) (2015) 114112.

[43] M. G. Martin, J. I. Siepmann, Transferable potentials for phase equilibria. 1. United-atom description of n-alkanes, Journal of Physical Chemistry B 102 (14) (1998) 2569–2577.

[44] D. J. Evans, B. L. Holian, The Nose–Hoover thermostat, The Journal of Chemical Physics 83 (8) (1985) 4069–4074.

[45] D. Dockar, L. Gibelli, M. K. Borg, Forced oscillation dynamics of surface nanobubbles, The Journal of Chemical Physics 153 (18) (2020) 184705.

[46] E. W. Lemmon, M. L. Huber, M. O. McLinden, et al., NIST standard reference database 23, Reference fluid thermodynamic and transport properties (REFPROP), version 9.

[47] G. Chen, S. Lu, K. Liu, Q. Xue, C. Xu, S. Tian, J. Li, Y. Zhang, M. Tong, X. Pang, B. Ni, S. Lu, Q. Qi, Investigation of pore size effects on adsorption behavior of shale gas, Marine and Petroleum Geology 109 (May) (2019) 1–8.

[48] S. Vela, F. Huarte-Larrañaga, A molecular dynamics simulation of methane adsorption in single walled carbon nanotube bundles, Carbon 49 (13) (2011) 4544 – 4553.

[49] Y. Pang, X. Hu, S. Wang, S. Chen, M. Y. Soliman, H. Deng, Characterization of adsorption isotherm and density profile in cylindrical nanopores: Modeling and measurement, Chemical Engineering Journal 396 (2020) 125212.

[50] K. Zeng, P. Jiang, Z. Lun, R. Xu, Molecular simulation of carbon dioxide and methane adsorption in shale organic nanopores, Energy & Fuels 33 (3) (2019) 1785–1796.

[51] M. Pinheiro, R. L. Martin, C. H. Rycroft, A. Jones, E. Iglesia, M. Haranczyk, Characterization and comparison of pore landscapes in crystalline porous materials, Journal of Molecular Graphics and Modelling 44 (2013) 208 – 219.

[52] F. Yang, Z. Ning, H. Liu, Fractal characteristics of shales from a shale gas reservoir in the Sichuan Basin, China, Fuel 115 (2014) 378–384.

[53] H. Tanaka, M. El-Merraoui, W. A. Steele, K. Kaneko, Methane adsorption on single-walled carbon nanotube: A density functional theory model, Chemical Physics Letters 352 (5-6) (2002) 334–341.

[54] M. Sahini, M. Sahimi, Applications of percolation theory, CRC Press, 2003.